11th International Symposium on Turbulence and Shear Flow Phenomena (TSFP11)
Southampton, UK, July 30 to August 2, 2019

DECAYING TURBULENCE IN A SALT-STRATIFIED FLUID

Shinya Okino
Department of Mechanical Engineering and Science
Kyoto University
Kyoto-Daigaku Katsura, Nishikyo-ku, Kyoto 615-8540, Japan
okino.shinya.8n@kyoto-u.ac.jp

Hideshi Hanazaki
Department of Mechanical Engineering and Science
Kyoto University
Kyoto-Daigaku Katsura, Nishikyo-ku, Kyoto 615-8540, Japan
hanazaki.hideshi.5w@kyoto-u.ac.jp

ABSTRACT

Decaying turbulence in a salt-stratified fluid with Schmidt number of 700 is investigated by direct numerical simulation. When the stratification effect is sufficiently weak and the Ozmidov scale is far above the Kolmogorov scale, the density perturbation behaves like a passive scalar convected by isotropic turbulence, and the corresponding potential energy spectrum exhibits Batchelor's k^{-1} law in the viscous-convective subrange. In contrast, when the stratification effect is strong (i.e. after the Ozmidov scale becomes smaller than the Kolmogorov scale), the spatial distribution of potential energy shows large clouds of small structures, and the potential energy has a flat spectrum rather than the k^{-1} law. This phenomenon occurs since the potential energy near the Kolmogorov scale is significantly reduced by the counter-gradient vertical density flux persistently converting potential energy into kinetic energy. However, if the buoyancy effect reaches down to the Kolmogorov scale sooner than the initial potential-energy cascade completes, only the large-scale pancake structures of potential energy are observed and small-scale fluctuations are absent.

INTRODUCTION

The ocean and brackish lakes are often density-stratified due to both temperature and salinity when averaged in time, and their motion is crucially influenced by the buoyancy caused by the density difference of the water. For example, the buoyancy drives the global circulation of the deep ocean called thermohaline circulation, which transports a huge amount of heat and carbon and is directly related to climate change like global warming. Besides, the density stratification in a brackish lake severely degrades the water since the buoyancy suppresses the vertical mixing and the resulting hypoxia at the bottom water is fatal to aquatic organisms.

Since early times, turbulence in a density-stratified fluid been studied by numerical simulations (Riley, Metcalfe and Weissman, 1981; Métais and Herring, 1989) and laboratory experiments (Stillinger, Helland and Van Atta, 1983; Itsweire, Helland and Van Atta, 1986). In laboratory experiments, salt water is often used to generate the density stratification (Fincham, Maxworthy and Spedding, 1996; Praud, Fincham and Sommeria, 2005), but its dissipative scale (Batchelor scale) is too small to be resolved accurately by the measurement. The salinity has a very small diffusion coefficient, so that the salinity perturbations in a turbulent flow decay far more slowly than the velocity perturbations. The slowness of diffusion is usually quantified by the Schmidt number, which is the ratio of the kinematic viscosity of fluid ν^* to the diffusion coefficient κ^* (i.e. $Sc = \nu^*/\kappa^*$).

Batchelor (1959) showed that a high-Sc scalar convected by isotropic turbulence dissipates at the wavenumber of $k_B^* = Sc^{1/2} k_K^*$ (now called the Batchelor wavenumber), where $k_K^* (= (\varepsilon_K^*/\nu^{*3})^{1/4})$ is the Kolmogorov wavenumber (ε_K^* being the kinetic-energy dissipation rate). Thus, the smallest length scale of salinity perturbation ($Sc = 700$) would be $\sqrt{700} (\sim 26)$ times smaller than the Kolmogorov scale if the buoyancy effect is negligible. Batchelor also derived a famous k^{*-1} power spectrum of the scalar variance in the viscous-convective subrange ($k_K^* < k^* < k_B^*$), where k^* is the wavenumber. His predictions have been confirmed later by experiments (Gibson and Schwarz, 1963) and numerical simulations (Bogucki, Domaradzki and Yeung, 1997; Yeung, Xu, Donzis and Sreenivasan, 2004).

The Schmidt number dependence of stratified turbulence has been discussed by water channel experiments (Komori and Nagata, 1996), the rapid distortion theory (Hanazaki and Hunt, 1996), and direct numerical simulations (Gerz and Yamazaki, 1993; Okino and Hanazaki, 2019). However, there are neither experimental nor numerical studies which accurately resolve the density perturbations at the sub-Kolmogorov scales for a Schmidt number as high as 10^3. Indeed, most of the recent numerical studies of stratified turbulence were intended for high Reynolds numbers, assuming $Sc = 1$ (e.g. Bartello and Tobias, 2013; Maffioli and Davidson, 2016; de Bruyn Kops and Riley, 2019).

This paper describes the result of the direct numerical simulation of decaying turbulence in a salt-stratified fluid ($Sc = 700$) to fill the gap between the previous experiments

and numerical simulations. In particular, we have examined how the strength of stratification affects the turbulent distribution of density perturbation.

DIRECT NUMERICAL SIMULATION

We consider decaying turbulence in a density-stratified fluid with Schmidt number of 700. The density stratification is stable and uniform (i.e. $d\bar{\rho}^*/dz^* = \text{const.} < 0$, where $\bar{\rho}^*$ is the unperturbed density and z^* is the vertical coordinate). Decaying turbulence with the initial rms velocity of U_0^* and the initial integral length scale of L_0^* is analysed by direct numerical simulation. In the following, we outline the methodology since the configuration of the problem and the numerical procedure are same as Okino and Hanazaki (2019).

The temporal development of the flow is determined by the continuity equation, the Navier-Stokes equation with the Boussinesq approximation and the transport equation of the density perturbation $\rho'^*(=\rho^*-\bar{\rho}^*(z^*))$. They are non-dimensionalised by the length scale L_0^*, the velocity scale U_0^*, and the density scale $-L_0^* d\bar{\rho}^*/dz^*$ as follows:

$$\frac{\partial u_i}{\partial x_i} = 0, \tag{1}$$

$$\frac{\partial u_i}{\partial t} + u_j \frac{\partial u_i}{\partial x_j} = -\frac{\partial p'}{\partial x_i} + \frac{1}{Re_0}\frac{\partial^2 u_i}{\partial x_j^2} - \frac{1}{Fr_0^2}\rho'\delta_{i3}, \tag{2}$$

$$\frac{\partial \rho'}{\partial t} + u_j \frac{\partial \rho'}{\partial x_j} = \frac{1}{Re_0 Sc}\frac{\partial^2 \rho'}{\partial x_j^2} + u_3, \tag{3}$$

where the variables without an upper asterisk denote the non-dimensional quantities. Here, the Cartesian coordinates (x,y,z) and the velocity components (u,v,w) are also expressed as (x_1,x_2,x_3) and (u_1,u_2,u_3), respectively. The initial Reynolds and Froude numbers are defined by $Re_0 = U_0^* L_0^*/\nu^*$ and $Fr_0 = U_0^*/(N^* L_0^*)$, where $N^* = \sqrt{-(g^*/\rho_0^*)(d\bar{\rho}^*/dz^*)}$ is the Brunt-Väisälä frequency (g^*: gravitational acceleration, ρ_0^*: representative density of the fluid). In the present study, we investigate the Froude number dependence of the flow ($Fr_0 = 0.3, 1$ and 10), keeping the Reynolds number constant ($Re_0 = 50$).

The governing equations are solved by the Fourier spectral method under the periodic boundary condition with a period of 4π. The aliasing errors are removed by the 3/2-rule. We used 4096^3 grid points when $0 \le t \le 6$ and 2048^3 points when $6 \le t \le 30$ to resolve the smallest scale of density perturbation. Indeed, $k_{\max}/k_B \ge 1.55$ is satisfied during the simulation, where $k_{\max}$ is the maximum wavenumber. The non-linear terms and the buoyancy term are developed in time by the 4th-order Runge-Kutta method, while the diffusive terms are analytically time-integrated using the integrating factor.

The numerical simulation is executed using up to 1024 nodes of NEC SX-ACE in the Cyberscience Center of Tohoku University and the Earth Simulator Center of Japan Agency of Marine-Earth Science and Technology (JAMSTEC).

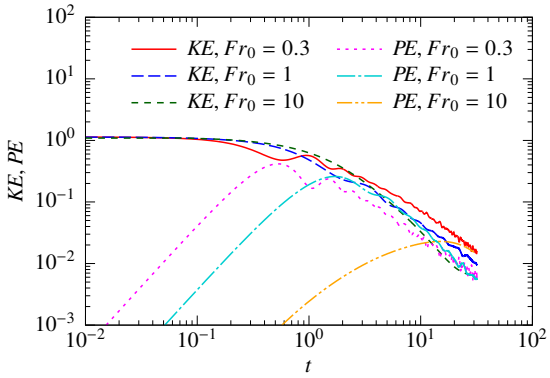

Figure 1. The temporal development of the kinetic and potential energies (*KE* and *PE*).

RESULTS

We first show in figure 1 the temporal development of the kinetic and potential energies, which are defined by $KE = \overline{u_i^2}/2$ and $PE = \overline{\rho'^2}/(2Fr_0^2)$, respectively, where the overline denotes the spatial average. The decay of the kinetic energy becomes slower for a smaller Froude number (stronger stratification), in agreement with Bartello and Tobias (2013). The initial growth of the potential energy is caused by the vertical density flux converting the kinetic energy into the potential energy. The time at which the potential energy becomes maximum is delayed for a larger Froude number (weaker stratification) since the Brunt-Väisälä period becomes longer and the energy conversion occurs more slowly. Indeed, the maximum potential energy occurs at $t \sim T_{BV}/4$, where the Brunt-Väisälä period $T_{BV} = 2\pi Fr_0$ in the non-dimensional form.

Figure 2(a) shows the temporal development of the Ozmidov and Kolmogorov wavenumbers, where the Ozmidov wavenumber is defined in dimensional form by $k_O^* = (N^{*3}/\varepsilon_K^*)^{1/2}$. The temporal variation of the Kolmogorov wavenumber hardly depends on the Froude number since the kinetic energy dissipation rate is insensitive to the stratification (cf. Bartello and Tobias, 2013). Meanwhile, as is easily anticipated by definition, the Ozmidov wavenumber becomes larger for a larger Froude number. The Ozmidov wavenumber increases with time, indicating that the buoyancy effect gradually prevails in smaller-scale motions as time passes. Since the Kolmogorov wavenumber is almost insensitive to the Froude number, the agreement between the Kolmogorov and Ozmidov wavenumbers is delayed for a larger Froude number. Indeed, they match at $t = 1.4$ for $Fr_0 = 0.3$ and $t = 7.2$ for $Fr_0 = 1$, and would match later than $t = 30$ for $Fr_0 = 10$.

Figure 2(b) shows the Froude number dependence of the buoyancy Reynolds number, which is defined by $Re_b = \varepsilon_K^*/(\nu^* N^{*2})$. The buoyancy Reynolds number is a measure of how the viscous dissipative scale is separated from the buoyancy affected scale since it is also expressed as $Re_b = (k_K^*/k_O^*)^{4/3}$. For $Fr_0 = 10$, the buoyancy Reynolds number is initially order of 10^3 and larger than unity even at $t = 30$, indicating that the flow is not significantly affected by the buoyancy. On the other hand, the buoyancy Reynolds number for $Fr_0 = 0.3$ falls below unity soon ($t = 1.4$), so that the flow would be mostly dominated by the buoyancy during the simulated time.

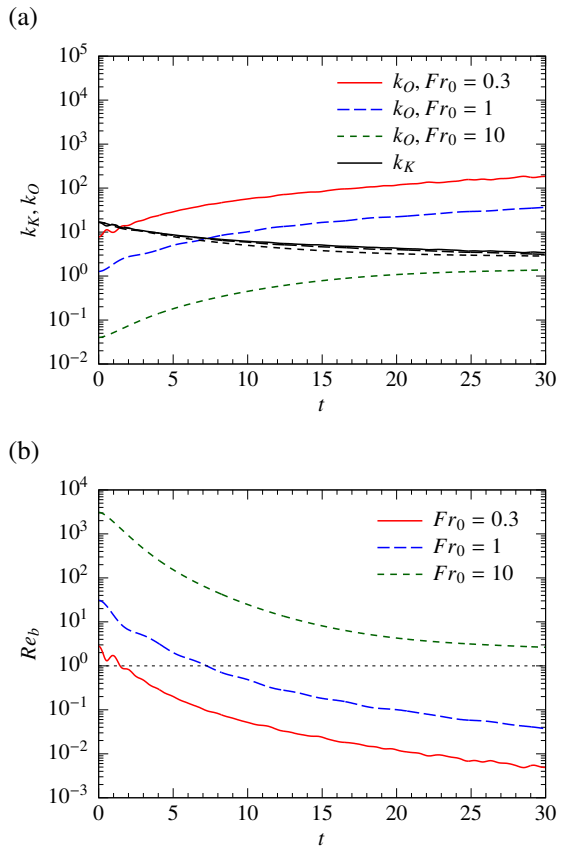

Figure 2. The temporal development of (a) the Ozmidov and Kolmogorov wavenumbers (k_O and k_K), and (b) the buoyancy Reynolds number (Re_b).

Results for moderate stratification

We next focus on the moderately stratified case of $Fr_0 = 1$, and describe the temporal variation of the potential energy distribution both in physical and wavenumber spaces.

Figure 3 illustrates the spatial distribution of the potential energy at two different times ($t = 4$ and 20). At an early time of $t = 4$ (figure 3a), the distribution appears to be isotropic and unaffected by stratification since the Ozmidov wavenumber ($k_O = 3.9$) is smaller than the Kolmogorov wavenumber ($k_K = 9.5$) and the buoyancy Reynolds number exceeds unity. Much later at $t = 20$ (figure 3b), even the smallest scale of fluid motion is affected by stratification since the Ozmidov wavenumber ($k_O = 22$) is far above the Kolmogorov wavenumber ($k_K = 4$). Then, the large-scale structures of the potential energy show pancake structures whose horizontal and vertical dimensions are comparable to the integral scales ($L_H = 2.2$ and $L_V = 1.2$). Here, the horizontal and vertical integral scales are defined respectively by

$$L_H = \frac{\pi \int dk_y \int dk_z |\hat{u}(0,k_y,k_z)|^2}{\overline{u^2}}, \tag{4}$$

and

$$L_V = \frac{\pi \int dk_x \int dk_y |\hat{w}(k_x,k_y,0)|^2}{\overline{w^2}}, \tag{5}$$

(e.g. Bradshaw 1971), where $\boldsymbol{k} = (k_x, k_y, k_z)$ is the wave vector, and $\hat{}$ denotes the Fourier component. The close-up view of each pancake structure (figure 3c) reveals that it is a *cloud* of vertically-thin sheets and streaks.

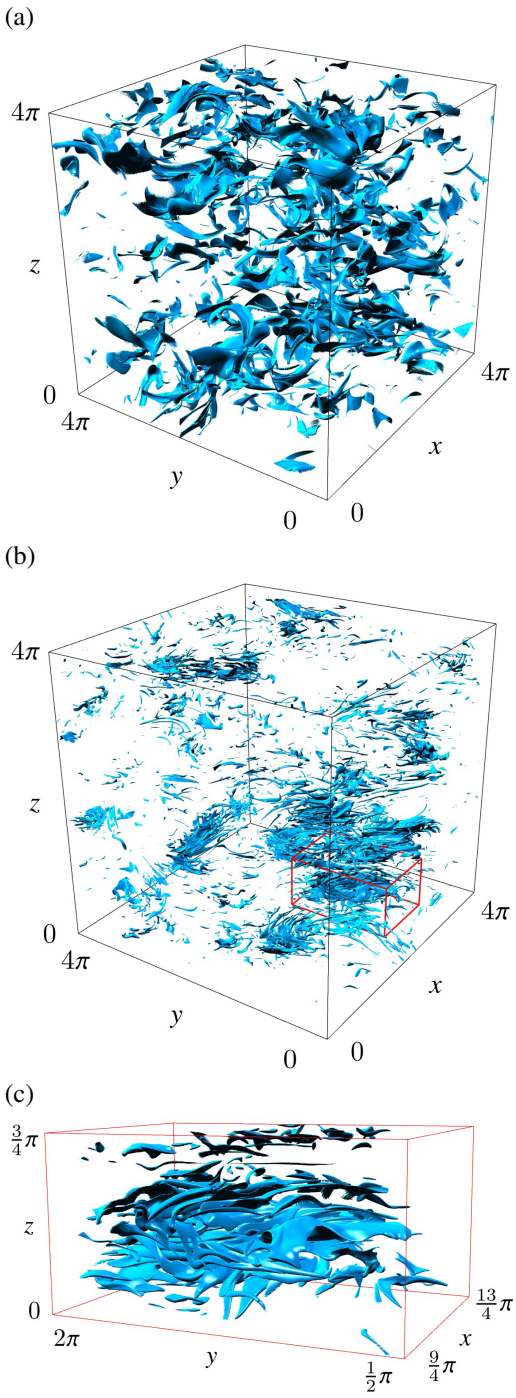

Figure 3. Spatial distributions of the potential energy with $Fr_0 = 1$ at (a) $t = 4$ and (b) $t = 20$. The isosurfaces of $\rho'^2/(2Fr_0^2) = 8PE$. (c) Close-up view of the red rectangular region in panel (b).

We present in figure 4(a) the time development of the radial spectrum of the potential energy, which is defined by

$$E_P(k) = \sum_{|\sqrt{k_x^2+k_y^2+k_z^2}-k|<k_{\min}/2} \frac{1}{2Fr_0^2} |\hat{\rho}'(k_x,k_y,k_z)|^2 \cdot \frac{1}{k_{\min}}, \tag{6}$$

where $k_{\min} = 0.5$ since the computational domain possesses

the periodicity of 4π. The variation of the Kolmogorov, Ozmidov and Batchelor wavenumbers are also indicated in the figure, for the same period of $4 \le t \le 20$.

Figure 4(a) shows that the density fluctuations initially ($t = 4$) constitute a k^{-1} spectrum in the viscous-convective subrange ($k_K < k < k_B$). This agrees with the Batchelor's prediction for a high Schmidt-number passive scalar ($Sc \gg 1$) in isotropic turbulence, since the Ozmidov wavenumber is smaller than the Kolmogorov wavenumber and the buoyancy effect is negligible above the Kolmogorov wavenumber. As time proceeds, the Ozmidov wavenumber increases while the Kolmogorov wavenumber decreases, and the fluid motion is mostly affected by buoyancy after $k_O = k_K$ is realised at $t = 7.2$. At the same time, the potential-energy spectrum changes its form and begins to bend near $k = k_K$, and the spectrum becomes steep ($\propto k^{-3}$) for low wavenumbers ($k \lesssim k_K$), while it becomes flat ($\propto k^0$) for high wavenumbers ($k_K \lesssim k \lesssim k_B$).

When the spectrum is multiplied by the wavenumber k and plotted against $\log k$, the area below the curve of $kE_P(k)$ indicates the amount of potential energy. Figure 4(b) shows initially (at $t = 4$) a plateau corresponding to the k^{-1} spectrum in the viscous-convective subrange, but the potential energy near the Kolmogorov scale ($k \sim 6$) subsequently decreases, leaving two peaks at low and high wavenumbers. The low-wavenumber peak at $k \sim 1.5$ corresponds to the pancakes or clouds observed in figure 3(b), and the high-wavenumber peak at $k \sim 40$ would correspond to the small-scale structures constituting those clouds (figure 3c).

The clouds of small-scale structures (figure 3b,c) were not observed in the numerical simulations for Schmidt numbers up to 70 (Okino and Hanazaki, 2019) since the difference between the Batchelor wavenumber and the Kolmogorov wavenumber was too small to observe the separation between the two peaks in figure 4(b).

To investigate the origin of the significant decrease of potential energy near the Kolmogorov wavenumber, we consider the budget for the potential-energy spectrum, i.e.

$$\frac{\partial E_P(k)}{\partial t} = -D_P(k) + C_{\rho' w}(k) + T_P(k), \qquad (7)$$

where $D_P(k)$ is the potential-energy dissipation spectrum, $C_{\rho' w}(k)$ is the co-spectrum of the vertical density flux responsible for the exchange between the kinetic and potential energies and $T_P(k)$ is the potential-energy transfer spectrum.

All the terms on the right-hand side of (7) in their pre-multiplied form are plotted in figure 5 using the values at $t = 8$, i.e. when the potential energy near the Kolmogorov wavenumber has decreased significantly (cf. figure 4b). The potential-energy dissipation $-kD_P(k)$ has a negative peak near the Batchelor wavenumber ($k \sim 10^2$), but approximately balances with the positive energy-transfer spectrum $kT_P(k)$. On the other hand, the co-spectrum of the vertical density flux $kC_{\rho' w}(k)$ is persistently negative and counter-gradient near and above the Kolmogorov wavenumber ($k \gtrsim k_K \sim 7$), while it oscillates in time and changes sign at low wavenumbers. This phenomenon has been observed in previous studies for high-Sc scalars (Komori and Nagata, 1996; Hanazaki and Hunt, 1996; Gerz and Yamazaki, 1993; Okino and Hanazaki, 2019), and the present results show that the persistent counter-gradient flux significantly reduces the potential energy near the Kolmogorov wavenumber.

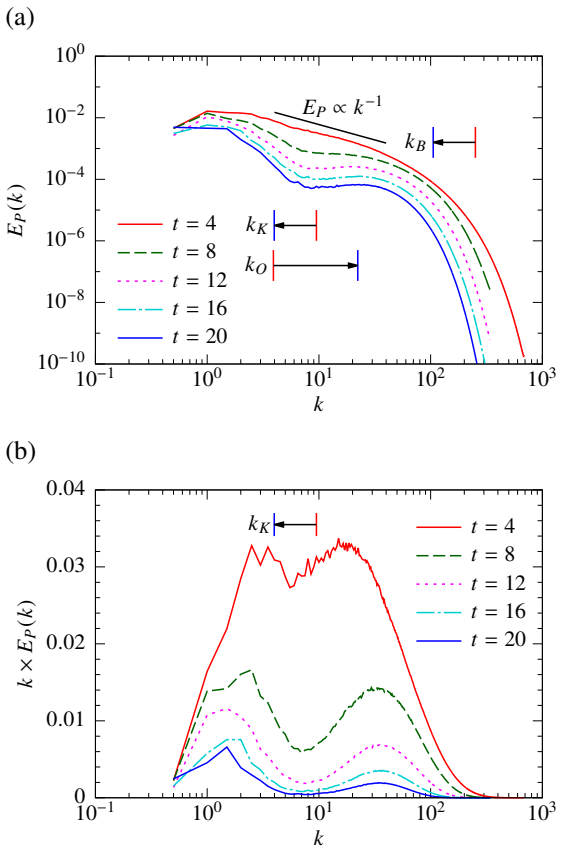

Figure 4. (a) Temporal variation of the potential energy spectrum $E_P(k)$ for $Fr_0 = 1$. Arrows indicate the temporal variation of the Kolmogorov, Ozmidov and Batchelor wavenumbers from $t = 4$ to $t = 20$. (b) Pre-multiplied spectrum of the potential energy, $k \times E_P(k)$, for $Fr_0 = 1$.

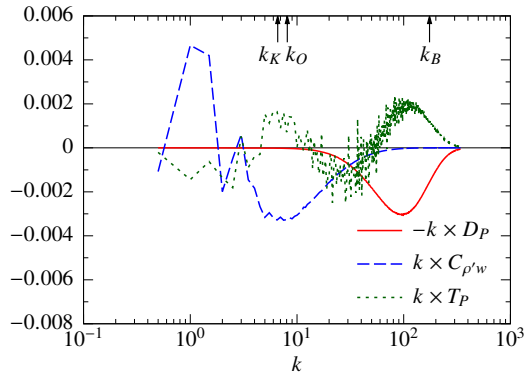

Figure 5. Spectral budget of the potential energy for $Fr_0 = 1$ at $t = 8$. The arrows show the Kolmogorov, Ozmidov, and Batchelor wavenumbers from the left.

Froude number dependence

We now examine the Froude number dependence of the potential-energy distribution. Figure 6 shows the spatial distributions of the potential energy for $Fr_0 = 10$ and 0.3 at $t = 20$. Under weak stratification of $Fr_0 = 10$, the Kolmogorov wavenumber is larger than the Ozmidov wavenumber and the buoyancy Reynolds number is larger than unity even in the final period of the simulation (figure 2a,b). Thus, the density perturbation would not be af-

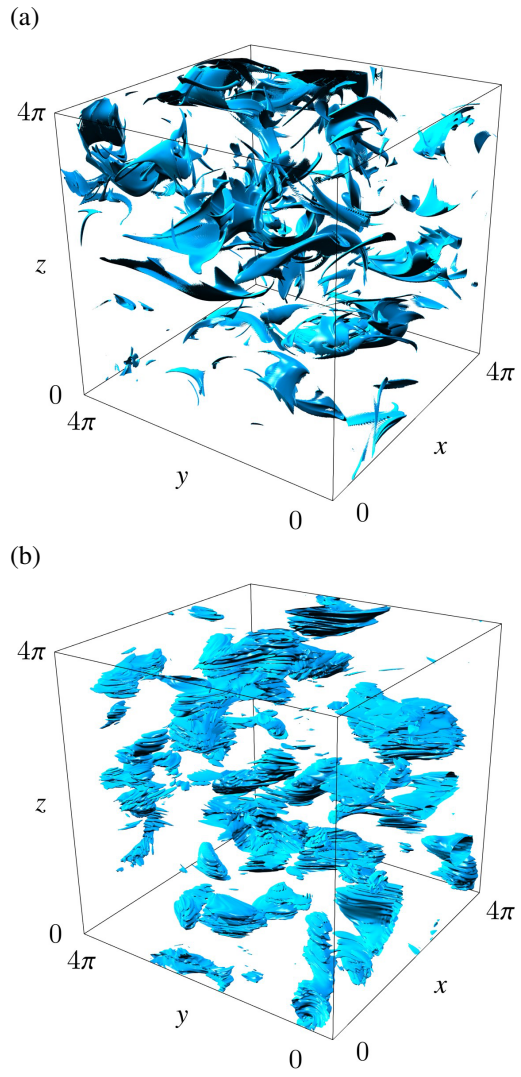

Figure 6. Spatial distributions of the potential energy with (a) $Fr_0 = 10$ and (b) $Fr_0 = 0.3$ at $t = 20$. The isosurfaces of (a) $\rho'^2/(2Fr_0^2) = 6PE$ and (b) $\rho'^2/(2Fr_0^2) = PE/3$.

fected largely by the buoyancy, and behave like a passive scalar. Indeed, as shown in figure 6(a), sheet-like structures of potential energy distribute isotropically (cf. Brethouwer, Hunt and Niewstadt, 2003). The distribution is also similar to figure 3(a), where the initial Froude number is smaller ($Fr_0 = 1$) and the time is much earlier ($t = 4$), but the buoyancy Reynolds number ($\sim 3 > 1$) is almost the same (figure 2b). Under strong stratification of $Fr_0 = 0.3$, the buoyancy Reynolds number at $t = 20$ is much smaller ($\sim 10^{-2}$). Then, small-scale fluctuations are absent and only the large-scale pancake structures with horizontal wrinkles are observed. Okino and Hanazaki (2019) explained that such a structure is generated by the vertically sheared horizontal flow at the Kolmogorov scale after the buoyancy Reynolds number falls below unity.

We finally show the temporal variation of the potential energy spectrum for $Fr_0 = 10$ and 0.3 in figure 7. For the case of $Fr_0 = 10$, the Ozmidov wavenumber is always larger than the Kolmogorov wavenumber, so that the buoyancy does not affect small-scale structures and Batchelor's k^{-1} law has been observed during the simulated time (figure 6a). The pre-multiplied spectrum in figure 7(c) shows that density perturbations as small as the Kolmogorov scale possess a large fraction of the potential energy and the plateau corresponding to the k^{-1} law is sustained for a long time. In contrast, the potential energy spectrum for $Fr_0 = 0.3$ does not have a constant slope of -1 since the buoyancy dominates small-scale motion from a very early time ($k_K < k_O$ at $t \gtrsim 2$. cf. figure 2a). Similar to the moderately stratified case ($Fr_0 = 1$), the potential energy spectrum bends near the Kolmogorov wavenumber (figure 7b) because the vertical density flux reduces the potential energy by converting it into the kinetic energy. The pre-multiplied spectrum in figure 7(d) appears quite different from that for $Fr_0 = 1$ (figure 4b) in that the pre-multiplied spectrum for $Fr_0 = 0.3$ has a single peak at $k \sim 2$ and lacks the second peak at the sub-Kolmogorov scale that was observed for $Fr_0 = 1$. This is because the energy conversion through the vertical density flux occurs sooner than the initial potential energy cascade down to the Batchelor wavenumber completes. Thus, small-scale fluctuations of the potential energy are absent for $Fr_0 = 0.3$ and only the large-scale pancake structures were observed in figure 6(b).

CONCLUSIONS

We have investigated decaying turbulence in a salt-stratified fluid ($Sc = 700$) for three Froude numbers ($Fr_0 = 0.3, 1$ and 10) using the direct numerical simulation.

When the stratification effect is sufficiently weak and the Ozmidov scale is far above the Kolmogorov scale (i.e. the buoyancy Reynolds number is large), the flow is not largely affected by the buoyancy. Then, the density perturbation behaves like a passive scalar convected by isotropic turbulence and the corresponding potential energy spectrum exhibits Batchelor's k^{-1} law in the viscous-convective subrange ($k_K \lesssim k \lesssim k_B$).

In contrast, when the stratification effect is strong (i.e. the buoyancy Reynolds number is smaller than unity), persistently negative (counter-gradient) vertical density flux converts the potential energy near the Kolmogorov scale into the kinetic energy. Then, the spatial distribution of potential energy shows large clouds of small structures, and the potential energy has a flat spectrum rather than the k^{-1} law. However, if the buoyancy effect reaches down to the Kolmogorov scale sooner than the initial potential-energy cascade completes, only the large-scale pancake structures of potential energy are observed and small-scale fluctuations are absent.

This study was supported by JSPS KAKENHI grant no. 18K13685, and used computational resources provided by Tohoku University through the HPCI System Research Project (hp170082, hp180092) and by the Earth Simulator Center of JAMSTEC.

REFERENCES

Bartello, P. & Tobias, S. M. 2013 Sensitivity of stratified turbulence to the buoyancy Reynolds number, *J. Fluid Mech.* **725**, 1–22.

Batchelor, G. K. 1959 Small-scale variation of convected quantities like temperature in turbulent fluid, *J. Fluid Mech.* **5**, 113–133.

Bogucki, D., Domaradzki, J. A. & Yeung, P. K. 1997 Direct numerical simulations of passive scalars with $Pr > 1$ advected by turbulent flow, *J. Fluid Mech.* **343**, 111–130.

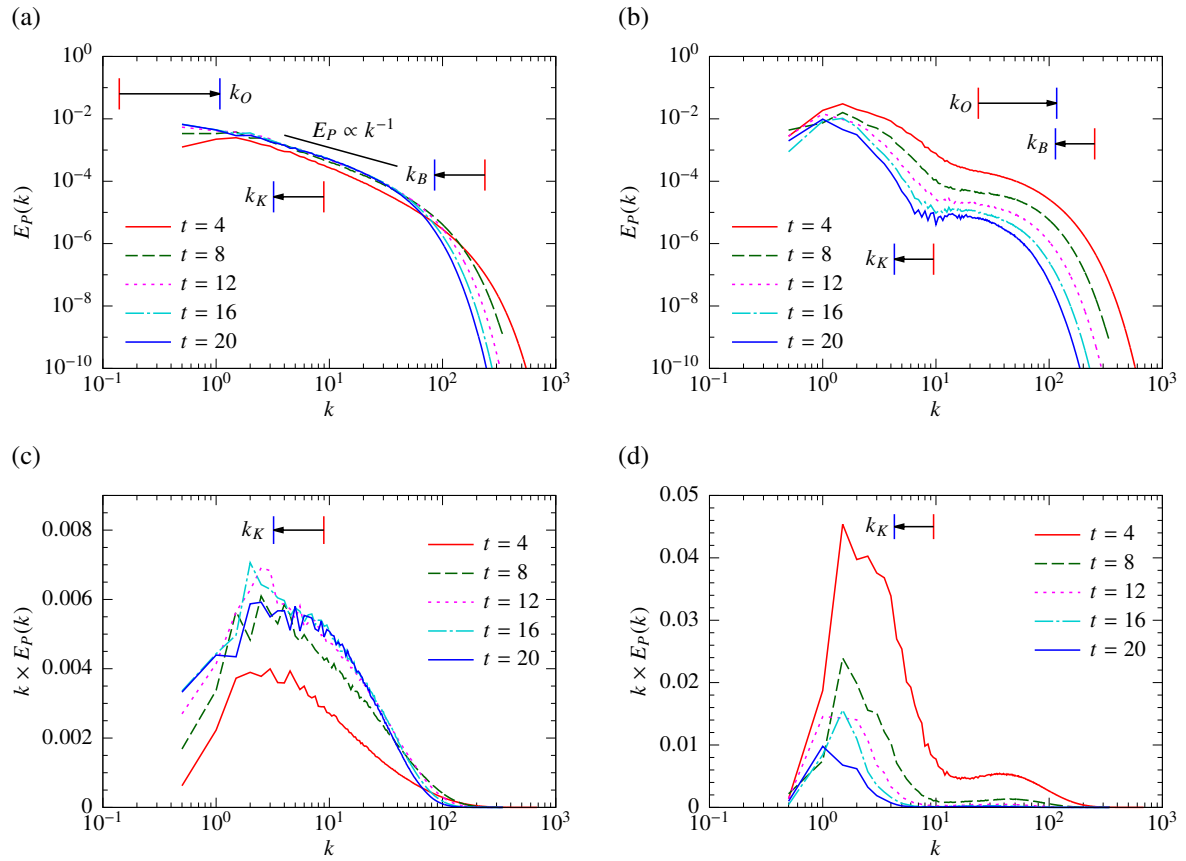

Figure 7. Temporal variation of the potential energy spectrum $E_P(k)$ for (a) $Fr_0 = 10$ and (b) $Fr_0 = 0.3$. Arrows indicate the temporal variation of the Kolmogorov, Ozmidov and Batchelor wavenumbers from $t = 4$ to $t = 20$. Pre-multiplied spectrum of the potential energy, $k \times E_P(k)$, for (c) $Fr_0 = 10$ and (d) $Fr_0 = 0.3$.

Bradshaw, P. 1971 *An Introduction to Turbulence and its Measurement*. Pergamon Press.

Brethouwer, G., Hunt, J. C. R. & Nieuwstadt, F. T. M. 2003 Micro-structure and Lagrangian statistics of the scalar field with a mean gradient in isotropic turbulence, *J. Fluid Mech.* **474**, 193–225.

de Bruyn Kops, S. M. & Riley, J. J. 2019 The effects of stable stratification on the decay of initially isotropic homogeneous turbulence *J. Fluid Mech.* **860**, 787–821.

Fincham, A. M., Maxworthy, T. & Spedding, G. R. 1996 Energy dissipation and vortex structure in freely decaying stratified grid turbulence, *Dynam. Atmos. Oceans* **23**, 155–169.

Gerz, T. & Yamazaki, H. 1993 Direct numerical simulation of buoyancy-driven turbulence in stably stratified fluid, *J. Fluid Mech.* **249**, 415–440.

Gibson, C. H. & Schwarz, W. H. 1963 The universal equilibrium spectra of turbulent velocity and scalar fields, *J. Fluid Mech.* **16**, 365–384.

Hanazaki, H. & Hunt, J. C. R. 1996 Linear processes in unsteady stable stratified turbulence, *J. Fluid Mech.* **318**, 303–337.

Itsweire, E. C., Helland, K. N. & Van Atta, C. W. 1986 The evolution of grid-generated turbulence in a stably stratified fluid, *J. Fluid Mech.* **162**, 299–338.

Komori, S. & Nagata, K. 1996 Effects of molecular diffusivities on counter-gradient scalar and momentum transfer in strongly stable stratification, *J. Fluid Mech.* **326**, 205–237.

Maffioli, A. & Davidson, P. A. 2016 Dynamics of stratified turbulence decaying from a high buoyancy Reynolds number, *J. Fluid Mech.* **786**, 210–233.

Métais, O. & Herring, J. R. 1989 Numerical simulations of freely evolving turbulence in stably stratified fluid, *J. Fluid Mech.* **202**, 117–148.

Okino, S. & Hanazaki, H. 2019 Decaying turbulence in a stratified fluid of high Prandtl number, *J. Fluid Mech.*, submitted.

Praud, O., Fincham, A. M. & Sommeria, J. 2005 Decaying grid turbulence in a strongly stratified fluid, *J. Fluid Mech.* **522**, 1–33.

Riley, J. J., Metcalfe, R. W. & Weissman, M. A. 1981 Direct numerical simulations of homogeneous turbulence in density-stratified fluids, *Proc. AIP Conf. on Nonlinear Properties of Internal Waves* (ed. Bruce J. West), 79–112.

Stillinger, D. C., Helland, K. N. & Van Atta, C. W. 1983 Experiments on the transition of homogeneous turbulence to internal waves in a stratified fluid, *J. Fluid Mech.* **131**, 91–122.

Yeung, P. K., Xu, S., Donzis, D. A. & Sreenivasan, K. R. 2004 Simulations of three-dimensional turbulence mixing for Schmidt numbers of the order 1000, *Flow Turbul. Combust.* **72**, 333–347.